Nonlinear Relationships of Fibrin Network Structure as a Function of Fibrinogen and Thrombin Concentrations for Purified Fibrinogen and Plasma Clots

Can Cai[1]*, Zezhong Zhang[1]*, Arezoo Nameny[1], Daniel Nelli[1], Keith Bonin[1], Brittany Bannish[2], Nathan E. Hudson[3], Glen Marrs[4], Stephen R. Baker[1†], Martin Guthold[1†]

[1] Department of Physics, Wake Forest University, Winston-Salem, NC 27109

[2] Department of Mathematics and Statistics, University of Central Oklahoma, Edmond, Oklahoma, 73034

[3] Department of Physics, East Carolina University, Greenville, NC 27885

[4] Department of Biology, Wake Forest University, Winston-Salem, NC 27109

* These authors contributed equally to this work.

[†] These authors are co-corresponding authors of this article.

Abstract

Background. Fibrinogen levels are associated with bleeding disorders and thrombotic disease. Thrombin converts fibrinogen to fibrin, producing the load-bearing fibrin scaffold that governs clot mechanics and transport.

Objective. Quantitatively map how fibrinogen and thrombin concentrations program fibrin architecture in human plasma and purified Peak 1 fibrinogen.

Methods. Scanning electron microscopy quantified single-fiber morphology—fiber diameter and branch-to-branch segment length from a standardized sample-preparation protocol. Confocal microscopy quantified network architecture (projected fiber density and pore/bubble size).

Results and Conclusions. Across plasma and purified systems, diverse readouts collapsed onto compact multiplicative scaling laws $Y = k[Fgn]_0^{\alpha}[Thr]_0^{\beta}$. The exponent patterns reveal a division of labor: thrombin primarily controls single-fiber growth kinetics, strongly shortening branch-to-branch segment length and modestly thinning fibers, whereas fibrinogen primarily controls space filling, strongly increasing fiber density and reducing pore/bubble size while thickening fibers. Network metrics further followed an approximately geometric packing relation (pore/bubble size $\propto$ fiber density$^{-1/2}$) across systems. For matched $[Fgn]_0$ and $[Thr]_0$, purified fibrinogen formed denser networks with smaller pores than plasma, consistent with environment-dependent effective assembly conditions. These parameterized scaling relations allow prediction linking composition to fibrin microstructure across plasma and purified fibrinogen clots, and they motivate a mechanistic picture in which thrombin sets the kinetic/length scale of single-fiber growth while fibrinogen tunes space-filling architecture. Fiber length analysis suggests that each thrombin molecule nucleates one fiber. These relationships provide the baseline for extensive, quantitative modeling work of blood clotting.

Introduction

Blood clotting is tightly regulated in space and time: clots must assemble rapidly and locally at sites of vascular injury to prevent blood loss, seal the wound, and limit infection. In bleeding disorders such as hemophilia and von Willebrand disease, impaired fibrin formation or platelet adhesion can yield delayed, undersized, mechanically weak clots that may fail to arrest bleeding. When clotting is initiated inappropriately or fails to undergo timely fibrinolysis, persistent thrombi in critical vascular beds such as the brain, heart, and deep veins can lead to ischemic stroke, myocardial infarction, and deep vein thrombosis [1, 2].

Fibrin fibers provide the load bearing scaffold of the clot. In the prevailing assembly model, thrombin cleaves fibrinopeptides A and B to expose binding sites termed 'knob A' and 'knob B' that drive knob-hole interactions, forming fibrin aggregates and half staggered protofibrils that elongate by end addition and thicken by lateral aggregation, a process influenced by the alpha C regions. As these bundles intersect, they form a branched, three-dimensional network. Abnormal fibrinogen levels are clinically relevant: elevated fibrinogen is associated with ischemic stroke, myocardial infarction, and venous thromboembolism, whereas reduced fibrinogen, for example in postpartum hemorrhage, predisposes to bleeding [3-5]. Thrombin generation is likewise central: insufficient thrombin, as in some types of hemophilia, causes hemostatic failure, while excessive or sustained thrombin, as in cancer associated thrombosis or antiphospholipid syndrome, promotes thrombosis [6-8]. Together, fibrinogen and thrombin set the structural state of the network, which in turn shapes clot mechanical behavior and susceptibility to lysis [1].

A persistent challenge is that published structure concentration relationships are difficult to compare across studies, even when the qualitative conclusions appear similar. For fiber diameter, most reports spanning confocal microscopy, SEM, and turbidimetry support an increase with fibrinogen, whereas a smaller set report the opposite trend [9-13]. Reported diameters also span a wide range, from tens of nanometers to micrometers [10-13]. This variability is not solely biological. It reflects differences in measurement resolution and in the analysis and modeling frameworks used to map protein concentration to structure. Confocal microscopy is diffraction limited and cannot resolve fiber diameters under about 300 nm [14]. SEM provides higher spatial resolution, but sample preparation steps such as washing, dehydration, and coating can alter apparent geometry [9, 11-13]. Light scattering relies on models that use restrictive approximations and can be less accurate when fibers are very thin or become very thick (on the order of the wavelength of light) or networks are highly heterogeneous [10]. As a result, studies have described diameter dependence using different functional forms, including approximately linear relations in some SEM analyses and nonlinear scaling consistent with power law behavior in scattering-based work [10, 12]. In contrast to the fibrinogen dependence, there is broader agreement that increasing thrombin produces thinner fibers, although the reported magnitude again varies across methods [9, 11-13].

Fiber length and pore scale metrics add further complexity because they are intrinsically harder to define and measure in images. Fiber segments commonly extend beyond the field of view, and apparent crossings in two-dimensional projections do not always correspond to true branch points, complicating segmentation and length assignment [15]. A prior confocal study quantified apparent lengths from single planes and reported shorter apparent lengths with increasing fibrinogen or thrombin [12]. However, a growing body of work indicates that structural features such as fiber diameter and length are not well described by normal distributions, motivating robust summary statistics and careful aggregation

across images [9, 16, 17]. For example, a standardized SEM study reported lognormal diameter distributions [17], and three-dimensional confocal reconstructions indicate lognormal like behavior for both diameter and length [9]. For network packing, fiber density has been estimated from confocal images using intensity-based measures [12] and from light scattering through inference of structural parameters [10]. Pore size is often quantified from confocal data using a largest inscribed circle or bubble analysis that yields a pore diameter distribution [18], alongside alternative estimators such as chord length intercepts or distance map-based approaches [19]. Across these approaches, a consistent qualitative trend is that higher fibrinogen or thrombin tends to reduce pore size, although the reported functional form varies between datasets and analysis choices [12, 18, 20, 21]. Despite extensive prior work describing how fibrinogen and thrombin influence fibrin network architecture, the field still lacks a predictive and quantitatively transferable mapping from composition to structure that spans multiple structural metrics and can be reused across studies. In practice, most reports emphasize qualitative trends (e.g., thicker versus thinner fibers) or provide method-specific absolute values that are difficult to reconcile because definitions, resolution limits, and preparation/analysis workflows differ. This limits mechanistic inference and modeling: without internally consistent scaling relationships for fiber diameter, segment-level length, network density, and pore size, it remains difficult to (i) test assembly hypotheses, (ii) link microstructure to mechanics and fibrinolysis, or (iii) calibrate and validate multiscale simulations of clot structure, mechanics, and transport.

Here we test the hypothesis that fibrin architecture across a fibrinogen–thrombin condition matrix follows a common *nonlinear scaling* form that can be expressed compactly by power-law relationships. We place plasma and purified systems on the same biochemical coordinate system (fibrinogen × thrombin), enabling direct cross-system comparisons and revealing a robust system-dependent shift in the scaling prefactor k, consistent with plasma-dependent modulation of the baseline microstructural scale at fixed $[Fg]$ and $[Thr]$. We combine standardized, high-magnification SEM [17] to quantify fiber diameter and segment-level length with 3D confocal imaging to quantify fiber density and pore size (line-intercept crossing counts and slice-wise bubble analysis [18]). Using a shared power-law parameterization across metrics and systems, we derive a unified set of scaling equations that functions as a practical "structure calculator" for predicting network morphology and provides quantitative benchmarks for testing mechanistic assembly models and for validating computational simulations of fibrin and related fibrous hydrogels.

Materials & Methods

Reagents

Pooled normal human plasma (George King Bio-Medical, Product #0010) and Peak 1 human fibrinogen (Enzyme Research Laboratories, Cat# P1 FIB) were aliquoted and stored at −80 °C. Human thrombin (Enzyme Research Laboratories, Cat# HT1002a) was aliquoted and stored at −80 °C. Alexa Fluor 488–conjugated human fibrinogen (Thermo Fisher Scientific, Cat# F13191) was aliquoted and stored at −80 °C. Aliquots were thawed at 37 °C immediately before use.

SEM sample preparation and imaging

Clot conditions. Plasma clots were prepared at room temperature across a 4×4 matrix of fibrinogen (0.36, 0.73, 1.45, 2.9 mg/mL) and thrombin (0.05, 0.1, 0.2, 1.0 U/mL). Purified

(Peak 1) clots were prepared across a 3×3 matrix of fibrinogen (0.36, 0.73, 1.45 mg/mL) and thrombin (0.05, 0.1, 0.2 U/mL). Clotting was initiated by adding an activation mix containing thrombin and $CaCl_2$ to achieve the thrombin concentrations listed above in Tris-buffered saline (50 mM Tris, 100 mM NaCl, pH 7.4). $CaCl_2$ was included at 20 mM for plasma clots and 9.5 mM for purified fibrinogen clots. The higher $CaCl_2$ in plasma was used to recalcify citrated plasma (George King) and overcome citrate chelation, whereas purified fibrinogen contains no citrate; we therefore used 9.5 mM $CaCl_2$ in the purified system to keep the added Ca^{2+} in the same order of magnitude and facilitate comparison between plasma and purified conditions. Clots were allowed to polymerize for 2 h at room temperature.

Fixation, drying, and coating. Samples were prepared using a standardized wash–fix–dehydrate–dry workflow as previously described [17]. After polymerization, clots formed in Eppendorf tube lids were washed three times in sodium cacodylate buffer (50 mM sodium cacodylate, 100 mM NaCl) and then fixed by immersion in 2 mL of 2% glutaraldehyde prepared in the same buffer for 6 h. Following fixation, samples were washed three additional times in sodium cacodylate buffer, dehydrated through a graded ethanol series (30%-100%), and dried using hexamethyldisilazane (HMDS). Dried samples were sputter-coated with gold for 45 s (Cressington Model 108).

SEM imaging. Samples were imaged on a Zeiss Gemini 300 SEM under high vacuum at 30,000× magnification. For each condition, 16 images (randomly selected fields of view) were collected.

Confocal sample preparation and imaging

Clot conditions and sample preparation. For confocal experiments, plasma clots and purified fibrinogen (Peak 1) fibrin clots were prepared using a 3×3 matrix of fibrinogen (0.36, 0.73, and 1.45 mg/mL) and thrombin (0.05, 0.1, and 0.2 U/mL) in TBS (20 mM Tris, 150 mM NaCl, pH 7.4). $CaCl_2$ was included at 20 mM for plasma clots and 9.5 mM for purified fibrinogen clots, as described in SEM part above. Alexa Fluor 488–fibrinogen was incorporated at 6.5% of the total fibrinogen concentration. Immediately before use, the labeled fibrinogen was warmed and briefly centrifuged (10 s) to remove aggregates. Reactions were loaded into channel slides (ibidi μ-Slide VI 0.4), shielded from light, and allowed to polymerize for 2 h at room temperature.

Confocal imaging. Imaging was carried out on a Zeiss LSM 710 laser-scanning confocal microscope with a 40× oil-immersion, 1.3 NA objective lens using 488 nm excitation light. For each condition, 36 z-stacks were collected (18 per slide from two slides). Each slide contained six channels; three imaging positions per channel were selected at random, spaced several millimeters apart and positioned 3–6 μm away from channel edges to reduce boundary effects. Stacks spanned 212 μm × 212 μm in x–y and 15 μm in z (33 optical sections, 0.47 μm step size) and were acquired at 8-bit depth. Detector gain was tuned to clearly resolve fibers while minimizing background signal.

Image analysis and quantitative network metrics

Fiber diameter. An ImageJ-based manual approach was used to quantify fiber diameter. Briefly, an evenly spaced grid was overlaid on each image, and fibers intersecting (or closest to) each grid crossing were selected for measurement, ensuring that each fiber was measured only once. At least 70 fibers were measured per image.

Fiber length. Using the grid-sampling method described above, fiber length was traced in ImageJ and defined as the distance along a fiber segment between adjacent branch points.

To avoid including truncated segments near the field boundaries, measurements were taken only within an interior region of interest defined by excluding a 10% margin from each image edge (i.e., fibers were measured only if they lay ≥10% of the image width/height away from the boundaries), while using the original, unaltered images. This corresponds to sampling the central 64% of the field of view. At least 30 fibers were measured per image.

Fiber density. Image stacks were converted to 2D maximum-intensity projections (ImageJ/Fiji) and then binarized using the same thresholding procedure across conditions. To estimate an in-plane fiber density, twenty horizontal and twenty vertical equally spaced line probes were overlaid on each projection, and the number of visible fibrin features intersecting each line was counted. Fiber density is reported as the mean number of intersections per 100 μm line.

Because each maximum projection was generated from a 15 μm z-stack, each 100 μm line integrates fluorescence from an effective 100 μm (length) × 15 μm (depth) sampling region; therefore, densities are reported as intersections per 1500 μm². A 15 μm acquisition depth was chosen as a practical compromise that yielded a high number of clearly resolvable, predominantly straight fiber features with minimal background.

This approach primarily captures resolvable fiber segments and is limited by confocal resolution and by the projection itself. In particular, very short segments (especially ≲1 μm) and closely spaced structures can be difficult to separate, and maximum-intensity projection can merge fibers along the optical axis. Consequently, the intersection count may be biased toward undercounting, especially in the densest networks (high fibrinogen/thrombin), where overlap is more frequent. Nevertheless, across most conditions, fibers were sufficiently separated to allow consistent identification of resolvable segments, and the same acquisition and analysis pipeline was applied to all samples to enable robust relative comparisons of fiber density.

Bubble analysis. Individual z-slices were exported as multi-page TIFFs and binarized in MATLAB using a threshold set to three times the mean slice intensity. Fiber-free pores were quantified with a custom algorithm that places the largest possible circles ("bubbles") within void regions on each slice, as described in Molteni et al [18, 22]. Circles that touched fibers, overlapped with larger accepted circles, or intersected the image boundary were discarded. The diameters of the remaining circles were recorded as a proxy for network porosity, where larger bubble diameters indicate larger pore/void regions. This analysis shares similar limitations to the projection-based fiber density measurement, including resolution/thresholding limits; the same pipeline was applied to all samples for consistent relative comparisons.

Curve fitting and statistical analysis

For each experimental condition, image-level measurements were summarized and related to the two experimental factors, fibrinogen concentration [Fgn] and thrombin concentration [Thr], using a power-law model:

$$Y = k\, F_0^{\alpha}\, T_0^{\beta},$$

where Y denotes the response variable (fiber diameter, fiber length, fiber density, or bubble diameter), F_0 and T_0 the initial fibrinogen and thrombin concentrations, and k, α, and β are fitted parameters. Model fitting was performed in log space by linear regression of

$$ln\,(Y) = ln\,(k) + \alpha ln\,([Fgn]) + \beta ln\,([Thr]),$$

using ordinary least squares (OLS). Goodness of fit was reported as R^2 computed in log space. Parameter uncertainty was quantified by 95% confidence intervals, and two-sided hypothesis tests were used to assess whether k, α and β differed from zero.
Because the distributions of fiber diameter, fiber length, and bubble diameter were non-Gaussian, these responses were summarized per condition using the median of image-level medians prior to model fitting. In contrast, fiber density was approximately normally distributed and was summarized per condition using the mean of image-level means prior to fitting.

Results

Purified (Peak 1) and plasma clots show distinct architectures across matched concentration matrices

Across the fibrinogen–thrombin matrices, SEM and confocal imaging reveal systematic changes in fibrin network architecture. Under comparable conditions, purified (Peak 1) clots form denser networks with smaller pores than plasma clots (Figs. 1 and 2), even though their fibers are thinner and shorter (Figs. 4 and 5). Overall, fibrinogen more strongly modulates fiber density and pore size, whereas thrombin more strongly influences fiber diameter and length. These differences are evident throughout the condition space rather than being driven by a single condition.

Power law fits quantify how fibrinogen and thrombin shape fibers and pores. To quantify concentration dependence, each structural metric was fit with a power law $Y = k[Fgn]^{\alpha}[Thr]^{\beta}$ (Figs. 3 and 6; Table 1 and 2); justification for power law fit, see discussion. The resulting exponents capture distinct contributions of fibrinogen and thrombin in both plasma and Peak 1 systems.
Fiber diameter (SEM). Fiber diameter increases with fibrinogen concentration and decreases with thrombin concentration in both plasma and Peak 1 clots. The same directional dependence is observed in both systems.
Fiber length (SEM). Fiber length shows a strong dependence on thrombin (shorter segments at higher thrombin) but weak sensitivity to fibrinogen. Consistent with this, the fitted fibrinogen exponent for length is small in both plasma and purified systems ($\alpha < 0.1$; Tables 1 and 2), yielding an almost flat trend versus fibrinogen compared with the thrombin dependence.
Fiber density and pore size (confocal). Confocal analysis showed that fiber density increases with both fibrinogen and thrombin, with fibrinogen having the stronger influence (Tables 1 and 2). In parallel, bubble diameter decreased with increasing fibrinogen and thrombin, indicating smaller pore spaces at higher concentrations.

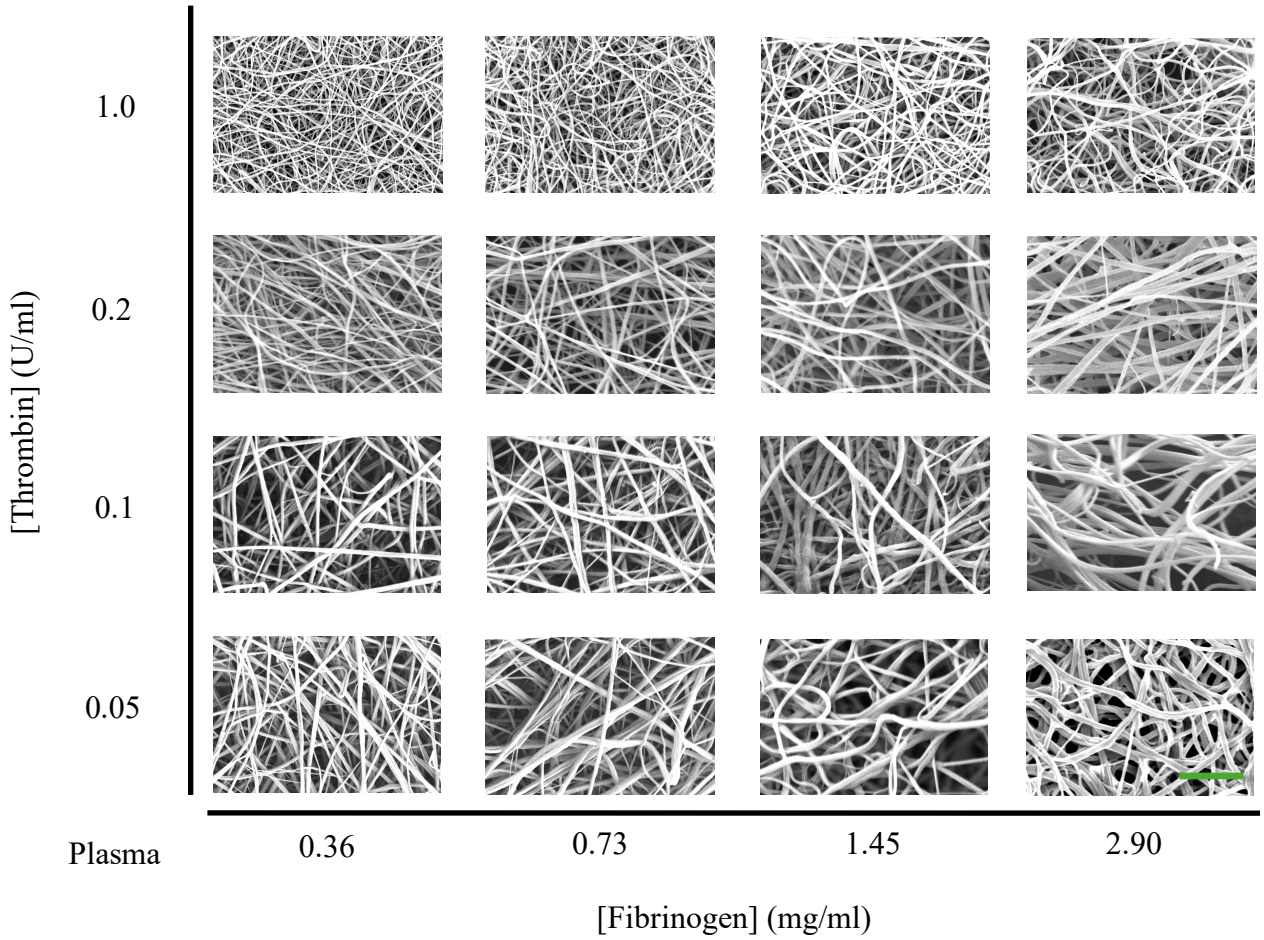

Figure 1: 4×4 matrix of representative SEM images showing plasma fibrin network structure across fibrinogen (x-axis) and thrombin (y-axis) concentrations. Each panel corresponds to a specific fibrinogen–thrombin condition. Scale bar: 1 µm.

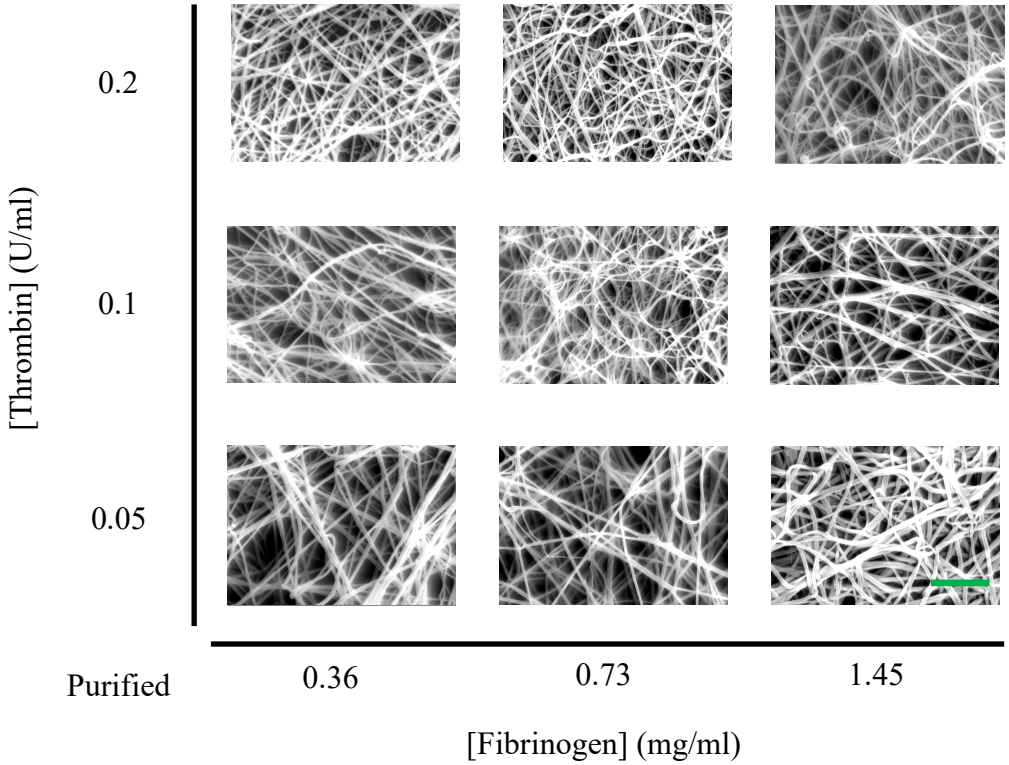

Figure 2: 3×3 matrix of representative SEM images showing purified (Peak 1) fibrin network structure across fibrinogen (x-axis) and thrombin (y-axis) concentrations. Each panel corresponds to a specific fibrinogen–thrombin condition. Scale bar: 1 µm.

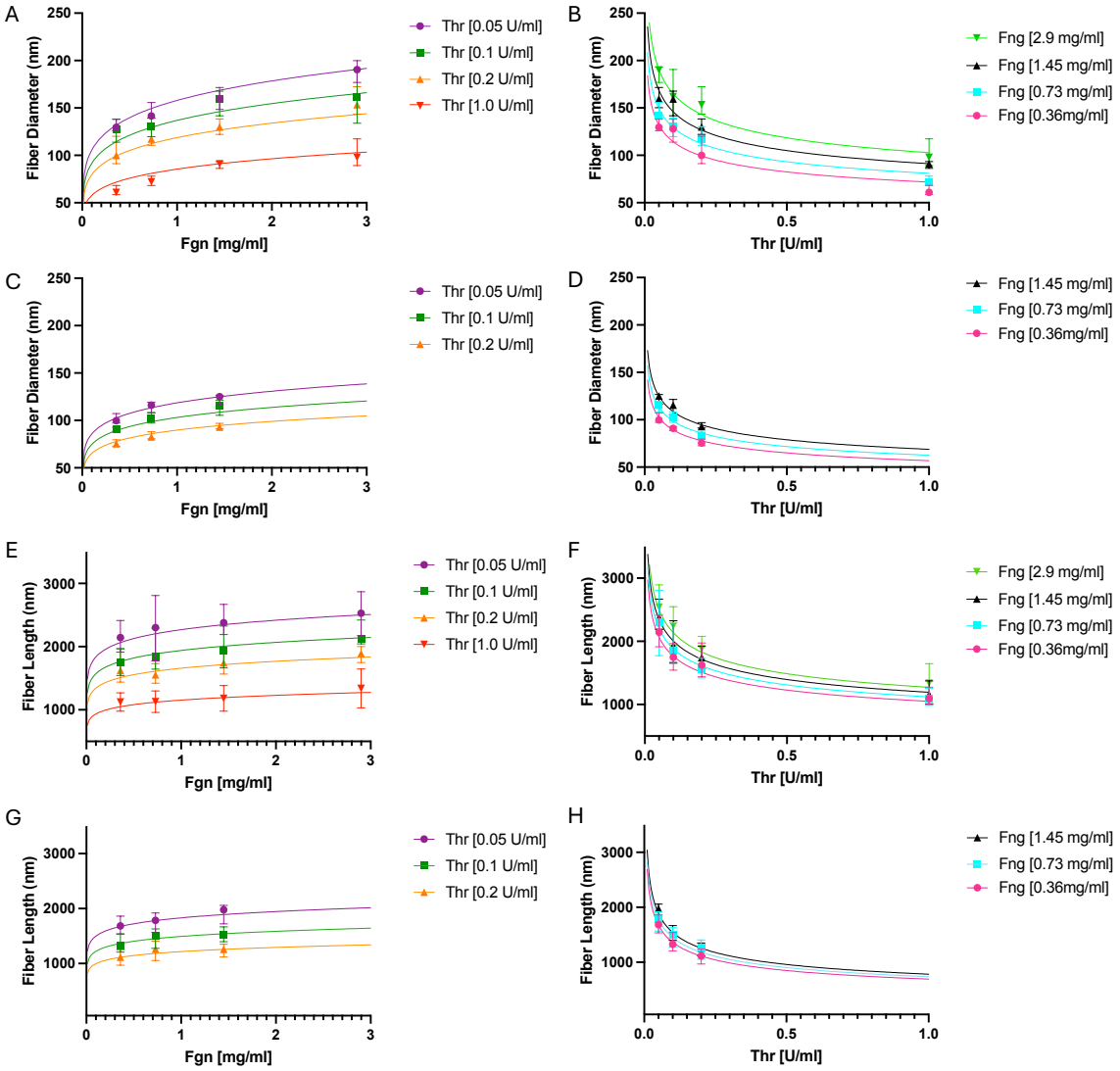

Figure 3: Concentration trends of fiber diameter and fiber length measured from SEM images, with power law fits. For each condition, fiber diameter and fiber length were summarized by the median. Solid lines indicate power law fits. Error bars show 95% confidence intervals across images within each condition. (A,B) Plasma fiber diameter vs fibrinogen and thrombin. (C,D) Purified (Peak 1) fiber diameter vs fibrinogen and thrombin. (E,F) Plasma fiber length vs fibrinogen and thrombin. (G,H) Purified (Peak 1) fiber length vs fibrinogen and thrombin.

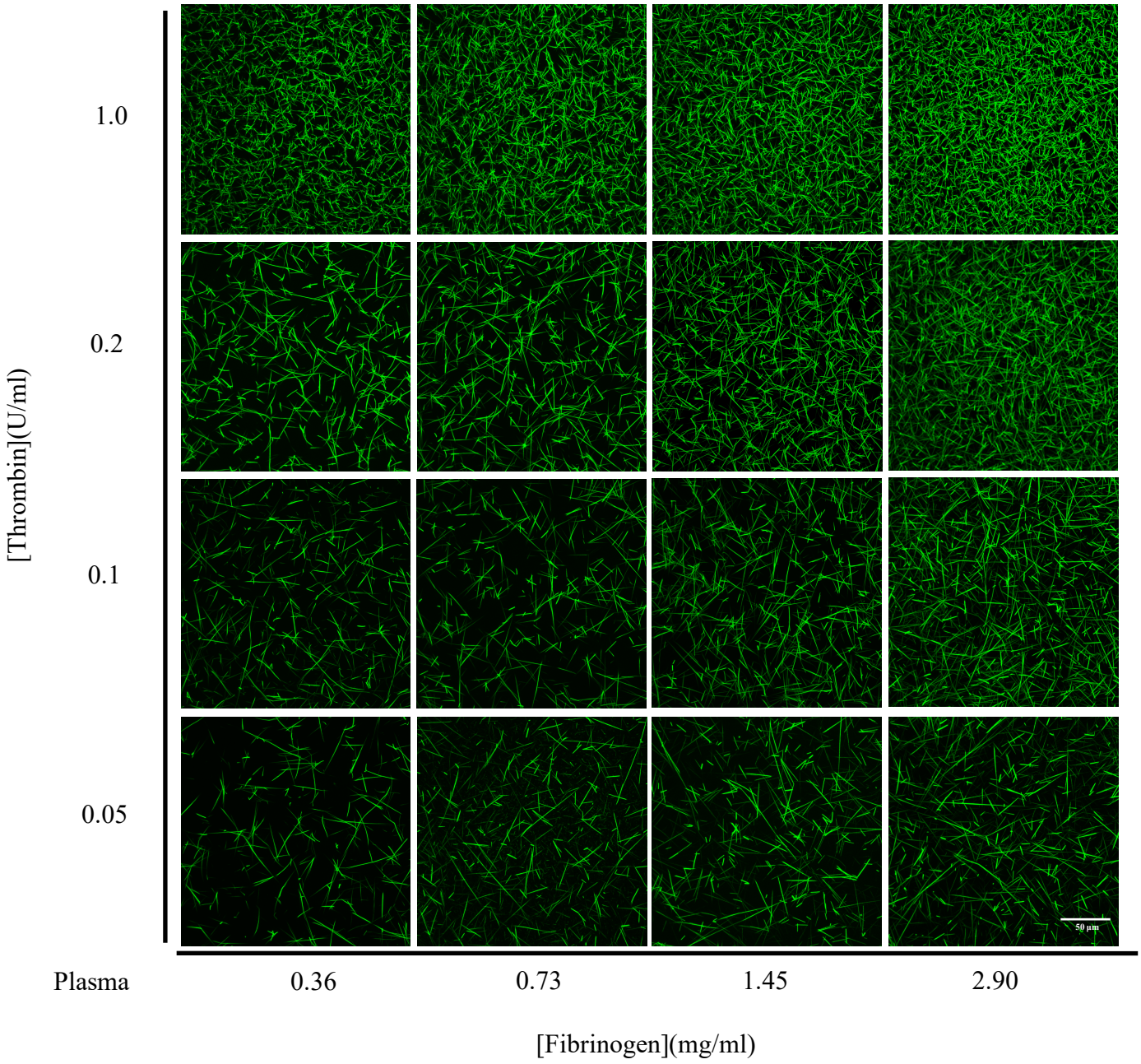

Figure 4: 4×4 matrix of representative confocal images showing plasma fibrin network structure across fibrinogen (x-axis) and thrombin (y-axis) concentrations. Each panel corresponds to a specific fibrinogen–thrombin condition. Scale bar: 50 µm.

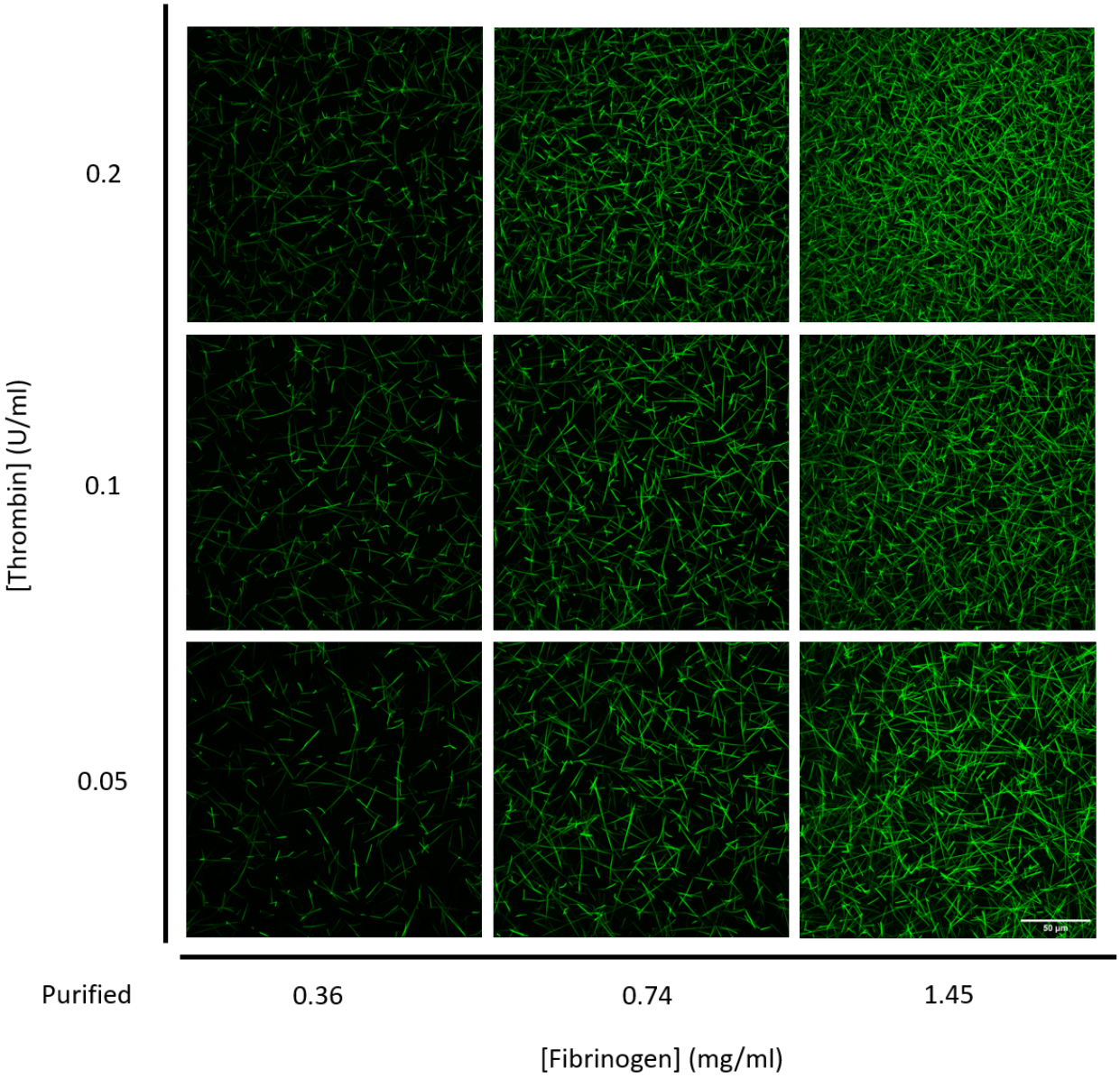

Figure5: 3×3 matrix of representative confocal images showing purified (Peak 1) fibrin network structure across fibrinogen (x-axis) and thrombin (y-axis) concentrations. Each panel corresponds to a specific fibrinogen–thrombin condition. Scale bar: 50 µm.

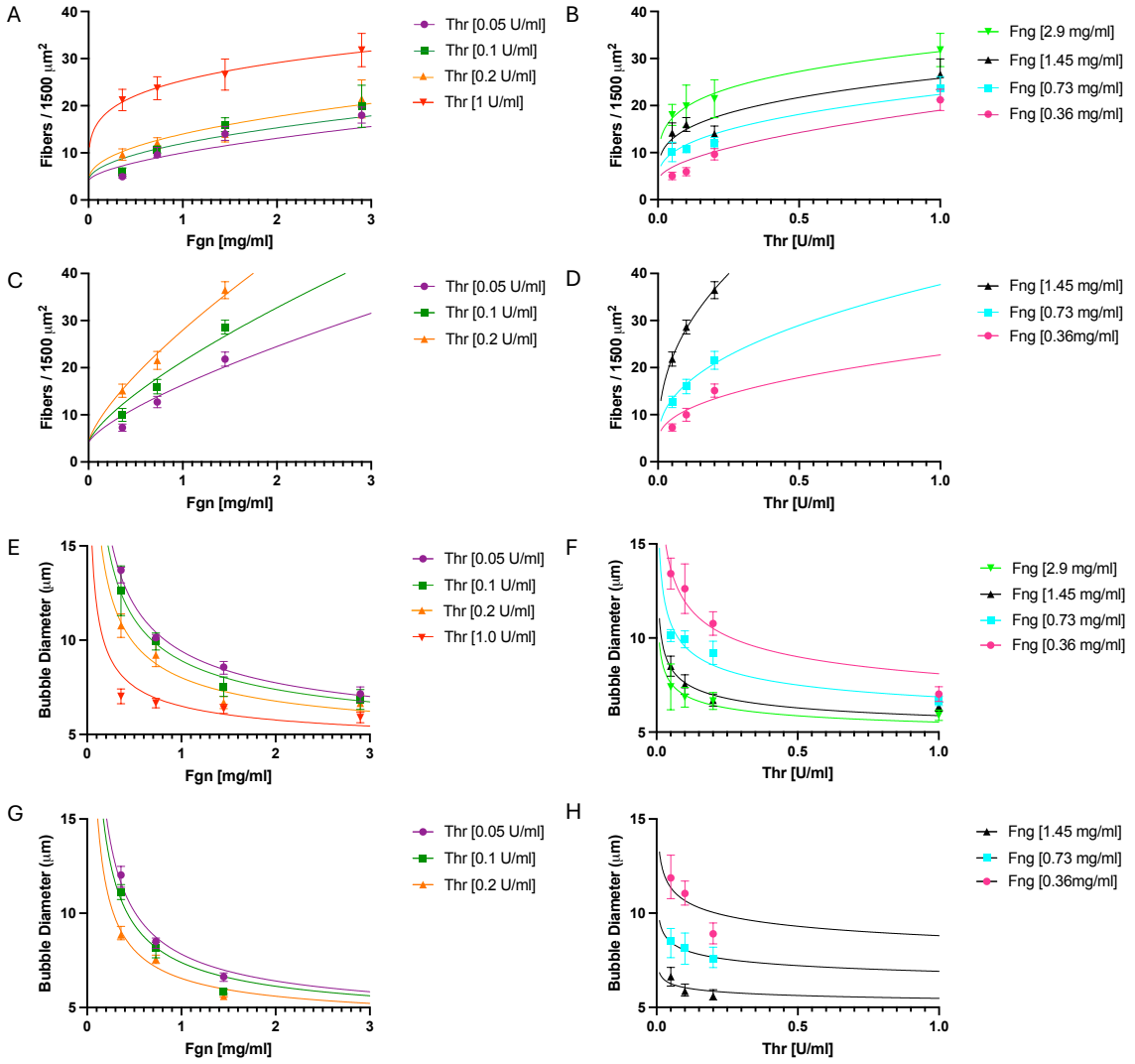

Figure 6: Concentration trends of fiber count and bubble diameter measured from confocal images, with power law fits. For each condition, fiber count was summarized by the mean, whereas bubble diameter was summarized by the median. Solid lines indicate power law fits. Error bars show 95% confidence intervals across images within each condition. (A,B) Plasma fiber count vs fibrinogen and thrombin. (C,D) Purified (Peak 1) fiber count vs fibrinogen and thrombin. (E,F) Plasma bubble diameter vs fibrinogen and thrombin. (G,H) Purified (Peak 1) bubble diameter vs fibrinogen and thrombin.

Plasma		Value	95% CI	P-Value	R^2 (log)
Parameters for Fiber diameter	k	81.20	[75.88, 86.65]	4.55e-22	0.95867
	α	0.19	[0.14, 0.24]	9.79e-7	
	β	- 0.23	[-0.26, -0.20]	1.30e-9	
Parameters for Fiber length	k	1154.51	[1065.74, 1249.03]	2.80e-12	0.96107
	α	0.092	[0.062, 0.12]	4.71e-5	
	β	-0.24	[-0.30, -0.17]	4.55e-5	
Parameters for Fiber density	k	25.09	[20.61, 30.56]	5.56e-09	0.88230
	α	0.45	[0.32, 0.59]	1.90e-05	
	β	0.30	[0.21, 0.40]	1.52e-03	
Parameters for Bubble diameter	k	6.57	[5.99, 7.20]	1.56e-15	0.88995
	α	-0.24	[-0.30, -0.17]	2.48e-06	
	β	-0.14	[-0.18, 0.091]	1.98e-05	

Table 1: Power-law fit parameters and statistical results for plasma fiber diameter, fiber length, fiber density, and bubble diameter using the model $Y = k\,[Fgn]^{\alpha}[Thr]^{\beta}$.

Purified Fibrinogen		Value	95% CI	P-Value	R^2 (log)
Parameters for Fiber diameter	k	63.65	[56.09, 72.22]	2.48e-10	0.95928
	α	0.15	[0.09, 0.20]	4.86e-4	
	β	- 0.21	[-0.26, -0.16]	6.74e-5	
Parameters for Fiber length	k	774.52	[571.60, 1049.24]	1.08e-5	0.84395
	α	0.071	[0.026, 0.12]	5.75e-3	
	β	-0.29	[-0.42, -0.16]	8.38e-3	
Parameters for Fiber density	k	56.67	[45.80, 70.14]	6.76e-09	0.98895
	α	0.73	[0.64, 0.81]	1.01e-06	
	β	0.43	[0.34, 0.52]	2.36e-05	
Parameters for Bubble diameter	k	5.06	[4.26, 6.02]	4.46e-7	0.97270
	α	-0.41	[-0.48, -0.33]	8.98e-06	
	β	-0.14	[-0.22, 0.070]	2.94e-03	

Table 2: Power-law fit parameters and statistical results for purified fiber diameter, fiber length, fiber density, and bubble diameter using the model $Y = k\,[Fgn]^{\alpha}[Thr]^{\beta}$.

Discussion

Mechanistic rationale for multiplicative power-law fits.

Across our concentration matrix, we found that many structural readouts Y (e.g., fiber diameter, length, density) are well described by

$$Y = k\,F_0^{\alpha}\,T_0^{\beta}, \qquad \text{(D1)}$$

where $F_0 \equiv [Fgn]_0$ is the initial fibrinogen concentration and $T_0 \equiv [Thr]_0$ is the initial thrombin concentration (input enzyme). The fitted exponents α, β are interpreted below as effective sensitivities over the finite assembly window rather than elementary reaction orders.

Activation and substrate depletion. Let $F(t)$ denote the remaining fibrinogen at time t, and let $r(t)$ denote the instantaneous rate (per unit volume) at which thrombin generates incorporation-competent fibrin species from fibrinogen. A minimal description is Michaelis–Menten (MM) kinetics with time-dependent effective thrombin activity:

$$r(t) = k_{\text{cat}}\, T_{\text{eff}}(t)\, \frac{F(t)}{K_m + F(t)}, 0 < T_{\text{eff}}(t) \leq T_0, \qquad \text{(D2)}$$

where k_{cat} and K_m are the usual MM parameters and $T_{\text{eff}}(t)$ is the effective thrombin concentration which accounts for inhibition and sequestration/binding effects [23]. Because fibrinogen is converted to fibrin, $F(t)$ decreases over the assembly window.

From production to growth interfaces. Let $N(t)$ denote the density of effective reactive growth interfaces at time t ("places where incorporation can occur", e.g., fiber ends or surface sites). A standard coarse-grained closure in polymerization is that, after a short transient, incorporation is fast enough that the free pool of incorporation-competent species does not accumulate; instead, it stays slaved to the production rate $r(t)$. Under this quasi-steady coarse-graining (details in Supplementary Note S1), the growth-interface creation can be written [15, 24] in the effective form

$$\frac{dN}{dt} = C\,[r(t)]^m\, N(t)^{-m}, \qquad \text{(D3)}$$

where m is an effective (generally positive) order summarizing the dominant association pathway(s) leading to new growth interfaces, and C collects rate constants. Integrating Eq. (D3) to a fixed readout time t_* gives

$$N(t_*)^{\,m+1} \propto \int_0^{t_*} r(t)^m\, dt. \qquad \text{(D4)}$$

Writing $T_{\text{eff}}(t) = T_0\, a(t)$ with $0 < a(t) \leq 1$ separates the thrombin input multiplicatively:

$$N(t_*) \propto T_0^{\frac{m}{m+1}}\, [I(F_0)]^{\frac{1}{m+1}}, I(F_0) \equiv \int_0^{t_*} a(t)^m \left(\frac{F(t)}{K_m + F(t)}\right)^m dt. \qquad \text{(D5)}$$

All time dependence—substrate depletion through $F(t)$ and thrombin inhibition/sequestration through $a(t)$—is contained in the single window functional $I(F_0)$. Because the MM factor $F/(K_m + F)$ smoothly interpolates between saturated (weak F-dependence) and linear (strong F-dependence) limits, the net fibrinogen dependence entering $I(F_0)$ is naturally summarized by a window-averaged effective exponent over our finite range of F_0. Finally, structural observables Y follow from geometric allocation of incorporated fibrin mass among $N(t_*)$ growth units (details in Supplementary Note S1), yielding the empirical form in Eq. (D1) with α, β as effective sensitivities.

A more complete derivation, including the quasi-steady reduction used to obtain Eq. (D3), the bounded log–log sensitivity of the MM factor, and explicit allocation examples (e.g., diameter), is provided in Supplementary Note S1.

Conserved fibrinogen and thrombin concentration sensitivities, and environment-dependent scaling (plasma vs purified system)

Across plasma and purified systems, the fitted power-law exponents are similar, indicating that the structural sensitivities to [Fgn] and [Thr] are largely conserved and consistent with a shared underlying assembly mechanism across our condition matrix. In contrast, the prefactor k changes substantially between systems. Because effective Ca^{2+} and NaCl concentrations were similar, a simple explanation for the change in k might be reduced effective thrombin activity in plasma due to thrombin consumption and inhibition (e.g., antithrombin, with contributions from α2-macroglobulin and heparin cofactor II). Consistent with a reduced effective thrombin activity in plasma [23], a turbidity study [12] reported markedly faster polymerization kinetics in a purified fibrinogen system compared to plasma under comparable conditions. Interpreting the change in k as a simple rescaling of thrombin activity yields an estimate that $[\mathrm{Thr}]_{\mathrm{eff}}$ may be reduced by 65–80% in plasma.

Kinetic control (thrombin) vs space-filling control (fibrinogen)

Our scaling analysis elucidates the different roles of thrombin and fibrinogen: thrombin primarily sets the gelation dynamics and thus the effective growth for individual fibers, whereas fibrinogen primarily sets how the network fills space. Mechanistically, increasing thrombin accelerates activation and early assembly, effectively increasing the rate at which assembly-competent species are generated and nucleation sites ("seeds") are generated. A higher density of nucleation sites means protofibrils, fibrin aggregates and early fibers encounter and connect with each other sooner, thereby advancing the percolation/gel point and shortening the time available for continued elongation of any single fiber. Consistent with this kinetic picture, fiber length is overwhelmingly thrombin-set—doubling thrombin *shortens* length by 15% in plasma ($2^{-0.24} = 0.85$) and 18% in purified/peak1fibrinogen ($2^{-0.29} = 0.82$), while doubling fibrinogen *increases* length by only 5–7% ($2^{0.071}$–$2^{0.092} = 1.05$–1.07)—arguing that elongation is limited by thrombin-controlled fiber progression rather than monomer-limited. In the same framework, a larger number of nucleation sites yields a higher fiber density, and the faster kinetic partitioning of a finite material supply among more growing units biases fibers toward being slightly thinner. Indeed, fiber density increases with thrombin (β = 0.30 in plasma; β = 0.43 in purified/peak1), while fiber diameter decreases with thrombin (β = −0.23 and −0.21, respectively).

In contrast, fibrinogen strongly influences the space-filling architecture: doubling fibrinogen increases fiber density by 37% in plasma ($2^{0.45}$ = 1.37) and 66% in purified/peak1 ($2^{0.73}$ = 1.66), while reducing bubble diameter by 15% in plasma ($2^{-0.24}$ = 0.85) and 25% in purified/peak1 ($2^{-0.41}$ = 0.75), respectively. Thrombin's effect on bubble diameter is comparatively small (9% per doubling; $2^{-0.14}$ = 0.91 in both systems). Notably, the fibrinogen exponent for bubble diameter is approximately half (with opposite sign) of the fibrinogen exponent for fiber density in both systems (−0.24/0.45 = −0.53; −0.41/0.73 = −0.56), implying a near-geometric packing relation bubble $\propto$ density$^{-1/2}$. The weaker density–fibrinogen scaling in plasma compared to purified fibrinogen (α = 0.45 vs 0.73) likely reflects that additional plasma constituents and regulation can partially mask a purely material-limited response in this metric. A similar effect may contribute to the weaker bubble–fibrinogen scaling in plasma compared to purified fibrinogen (α = −0.24 vs −0.41). Finally, fiber diameter depends oppositely on fibrinogen and thrombin concentrations, increasing fibrinogen thickens fibers (+11–14% per doubling) while thrombin slightly thins fibers (−14–15% per doubling); so these effects can largely cancel, yielding a weak net diameter dependence even as fiber density and bubble size shift dramatically.

Space filling (volume fraction) is superlinear with fibrinogen and contracts with thrombin

The fiber volume fraction is defined as the ratio of the volume occupied by all fibrin fibers to the total observation volume,

$$\phi \equiv \frac{V_{\text{fibrin}}}{V_{\text{tot}}}. \qquad \text{(D6)}$$

Approximating each fiber as a cylinder of diameter d and effective length l, the volume per fiber is $(\pi/4)d^2 l$. If N is the total number of fibers in the observation volume, then

$$\phi = \frac{N\left(\frac{\pi}{4}d^2 l\right)}{V_{\text{tot}}} = \rho\,\frac{\pi}{4}d^2 l, \qquad \text{(D7)}$$

where $\rho \equiv N/V_{\text{tot}}$ is the 3D fiber number density.

In our experiments we directly measure the projected (2D) fiber density

$$\sigma \equiv \frac{N}{A}, \qquad \text{(D8)}$$

where A is the projected imaging area. For an isotropic, space-filling network, dimensional consistency implies $\sigma = \rho^{2/3}$, and hence

$$\rho = \sigma^{3/2}. \qquad \text{(D9)}$$

Combining Eqs. (D7)–(D9) gives an expression for the volume fraction in terms of measured quantities,

$$\phi \propto \sigma^{3/2} d^2 l. \qquad \text{(D10)}$$

Equation (D10) contains only quantities we measure (σ, d, l), so it directly enables an empirical test of how the fiber volume fraction scales with fibrinogen and thrombin.

Under the simplest "mass supply" expectation—homogeneous fiber material density and conversion set primarily by fibrinogen availability—one would anticipate ϕ to increase linearly with F_0 (more fibrinogen ⇒ more fibrin volume) and to be independent of T_0 (thrombin reshapes morphology but does not itself contribute fiber volume). Writing the measured power-law scalings $\sigma \propto F_0^{\alpha_\sigma} T_0^{\beta_\sigma}$, $d \propto F_0^{\alpha_d} T_0^{\beta_d}$, and $l \propto F_0^{\alpha_l} T_0^{\beta_l}$, Eq. (D10) implies

$$\alpha_V = \frac{3}{2}\alpha_\sigma + 2\alpha_d + \alpha_l \quad \text{and} \quad \beta_V = \frac{3}{2}\beta_\sigma + 2\beta_d + \beta_l \qquad \text{(D11)}$$

where $\phi \propto F_0^{\alpha_V} T_0^{\beta_V}$.

Using the fitted exponents in Table 1 yields $\alpha_V = 1.147$ and $\beta_V = -0.25$ in plasma, and $\alpha_V = 1.466$ and $\beta_V = -0.07$ in purified fibrinogen. If increasing fibrinogen simply increased fiber volume at fixed fiber density, one would expect $\alpha_V \simeq 1$. Instead, $\alpha_V > 1$, consistent with fibrinogen driving a shift toward thicker fibers accompanied by reduced internal fiber mass density (thicker fibers have lower mass density), as observed previously [25]. In contrast, β_V is close to zero in purified fibrinogen, supporting the idea that thrombin primarily redistributes morphology/partitioning of single fibers rather than increasing or decreasing the total fiber volume fraction. The negative β_V in plasma indicates that a shift toward thinner fibers is accompanied by increased fiber mass density (thinner fibers have higher mass density). In this regime, fiber overlap and finite confocal resolution can cause σ (the measured projected density).

Why fiber segment length is mainly dependent on thrombin? Agreement between fiber segment length and space per thrombin molecule suggests a one-fiber-per-thrombin picture.

To relate the measured 3D branch-to-branch segment length, L_{seg}, to a spatial control parameter, we converted thrombin activity (NIH U/mL) into a thrombin molecular number density, ρ_{Thr}, using the lot-specific activity (3044 NIH U/mg). For the used lot, 1 NIH U/mL corresponds to ~ 9 nM thrombin, giving $\rho_{\text{Thr}} \approx 5.42\ \mu\text{m}^{-3}$ at 1 U/mL (and 1.08/0.542/0.271 μm^{-3} for 0.2/0.1/0.05 U/mL). From ρ_{Thr}we compute the mean volume per thrombin molecule, $V_{\text{part}} = 1/\rho_{\text{Thr}}$. Representing V_{part} as a cube provides a simple geometric spacing scale: the cube side is $L_{\text{cube}} = V_{\text{part}}^{1/3} = \rho_{\text{Thr}}^{-1/3}$, and the cube diagonal is $L_{\text{diag}} = \sqrt{3}\, L_{\text{cube}}$. If segments are approximately straight over these length scales, then

L_{cube} and L_{diag} provide lower and upper bounds on the center-to-center spacing expected from the thrombin number density, so $[L_{\text{cube}}, L_{\text{diag}}]$ serves as a thrombin-implied spacing range.

We compared this spacing range to the measured L_{seg} in both plasma and purified fibrinogen clots. Because fibrinogen has only a minor effect on L_{seg}, we pooled L_{seg} values across fibrinogen conditions at a fixed thrombin level and compared the pooled L_{seg} range to $[L_{\text{cube}}, L_{\text{diag}}]$ for that thrombin level (Table 3). Strikingly, across thrombin concentrations, the pooled L_{seg} values lie in the same micrometer range as $[L_{\text{cube}}, L_{\text{diag}}]$, and both contract systematically as thrombin increases. This agreement supports a direct interpretation: at a given thrombin concentration, the average volume "assigned" to one thrombin molecule contains on the order of one fiber segment, so the characteristic segment length is set primarily by the thrombin-implied spacing.

One plausible mechanism is a "one-nucleation center-per-thrombin" picture in which each thrombin molecule (or a small local cluster acting as one effective center) locally generates a burst of assembly-competent fibrin that accumulates within its assigned volume and builds a short segment. Gelation then occurs as these locally formed segments elongate, thicken, fill space, and encounter neighboring segments; once segments meet, they connect and the network becomes mechanically locked into a percolated scaffold. In this view, the typical segment length is limited by the thrombin-set spacing between neighboring initiation regions, giving a simple geometric scaling $L_{\text{seg}} \sim \rho_{\text{Thr}}^{-1/3} \propto [Thr]^{-1/3}$ (up to the lot-specific unit conversion). By contrast, fibrinogen primarily modulates how much fibrin mass is available within each initiation volume—thereby affecting thickness, mass-per-length, and space-filling—without strongly shifting the characteristic segment-length scale set by thrombin spacing.

Thrombin Density (particles/μm^3)	**Space Range L_{cube} (µm), L_{diag} (µm)**	**Plasma L_{seg} range (µm)**	**Purified Fibrinogen L_{seg} range (µm)**
5.42 (1 U/mL)	[0.57, 0.99]	[1.09, 1.30]	
1.08 (0.2 U/mL)	[0.97, 1.69]	[1.55, 1.89]	[1.69, 1.98]
0.542 (0.1 U/mL)	[1.23, 2.12]	[1.75, 2.12]	[1.33, 1.52]
0.271 (0.05 U/mL)	[1.55, 2.68]	[2.14, 2.53]	[1.69, 1.98]

Table 3: Thrombin number density–implied spacing scale compared with measured 3D fibrin segment length. (particles$\cdot\mu\text{m}^{-3}$) denotes thrombin molecular number density derived from thrombin activity (NIH U $\cdot$ mL^{-1}; parentheses; lot activity 3044 NIH U $\cdot$ mg^{-1}). The spacing range $[L_{\text{cube}}, L_{\text{diag}}]$ is defined by $L_{\text{cube}} = \rho_{\text{Thr}}^{-1/3}$ and $L_{\text{diag}} = \sqrt{3}\, L_{\text{cube}}$. L_{seg} ranges (plasma and purified fibrinogen) are pooled across fibrinogen conditions at fixed thrombin.

Novelty and limitations

Although related questions have been explored previously using similar experimental modalities, the present study provides a substantially more comprehensive and internally consistent characterization of how fibrinogen and thrombin jointly shape fibrin architecture across both plasma and purified systems. Specifically, we systematically mapped a 4×4 matrix in human plasma and a 3×3 matrix in purified Peak 1 fibrinogen, enabling direct, factorial comparisons across a wide range of $[Fgn]-[Thr]$ combinations. Prior work typically examined a much smaller subset of conditions—for example, varying thrombin at fixed fibrinogen or vice versa—often yielding weak or purely phenomenological linear fits with limited explanatory power [12]. Importantly, our cross-system comparisons were performed at matched thrombin concentrations in plasma and purified fibrinogen, avoiding confounds introduced by using different initiators (e.g., thrombin in one system versus tissue factor in the other), which can obscure mechanistic interpretation [12].

A key technical advance is that single-fiber dimensions were quantified using a standardized SEM preparation and imaging protocol, providing high-resolution, quantitatively robust measurements of fiber diameter and branch-to-branch segment length. Optical approaches can reveal qualitative trends in diameter but are intrinsically limited by diffraction and labeling/thresholding artifacts, especially for submicron fibers, making diameter estimates approximate [14]. By contrast, SEM under a standardized protocol resolves fiber boundaries with sufficient precision to support reliable comparisons across conditions. Segment length has been particularly challenging to quantify with existing microscopy-based workflows [15]. Here we leveraged SEM at moderate magnification and analyzed only the central portion of each image to minimize edge truncation, while maintaining a short working distance to ensure that measured segments lie within a well-defined focal plane. This combination reduces common biases in segment-length measurements, especially those arising from fibers leaving the field of view or from depth ambiguity, and enables precise quantification of L_{seg}.

We note, however, that network-level metrics derived from confocal microscopy (fiber density and pore/bubble readouts) are subject to well-known limitations. Because the analysis relies on resolvable features in confocal images and on projections/binarization, these quantities should be interpreted as resolution-limited trends rather than absolute 3D ground-truth values, particularly in the densest networks where overlap can lead to undercounting or merged pores (as discussed in Methods). Nevertheless, confocal imaging provides an important advantage for network-level readouts such as fiber density and pore size: it quantifies the clot in a hydrated, near-native state, minimizing dehydration- and shrinkage-related distortions that can strongly affect apparent network compaction under electron-microscopy sample preparation. Finally, these methodological considerations may help explain discrepancies with prior reports based on 2D confocal single-plane measurements that concluded segment length decreases with increasing fibrinogen and thrombin [12]. In that study, increasing fibrinogen was reported to shorten apparent segment length, whereas we observe the opposite trend. At high network density, limited resolution and ambiguous identification of true branch points versus projected crossings or fiber pile-up can systematically bias 2D measurements toward shorter inferred segments. In contrast, our SEM-based analysis resolves intersections and branch points directly with

sufficient spatial resolution, supporting a more reliable assessment of how fibrinogen and thrombin modulate L_{seg} across plasma and purified fibrinogen systems.

Conclusion

Fibrin architecture emerges from coupled enzyme activation, substrate depletion, formation of growth interfaces, and geometric mass allocation, yet predicting how fibrinogen and thrombin jointly shape microstructure remains challenging. By mapping fibrin structure across fibrinogen–thrombin concentration matrices in human plasma and purified Peak 1 fibrinogen, we found that a broad set of readouts is well summarized by compact multiplicative power laws $Y = k[Fgn]_0^{\alpha}[Thr]_0^{\beta}$. We present a simplified, coarse-grained kinetic rationale (Michaelis–Menten activation with depletion and a quasi-steady reduction during the main assembly window) to motivate why separable, power-law-like sensitivities can emerge over a finite experimental range.

The exponent patterns expose a division of labor between thrombin and fibrinogen. Thrombin acts primarily as a single-fiber kinetic controller: increasing thrombin accelerates early assembly and progression to connectivity, compressing the effective growth window and shortening the characteristic branch-to-branch segment length, consistent with a spatial "territory" interpretation in which segment length contracts on a thrombin-set micrometer scale. Fibrinogen acts primarily as a space-filling controller, strongly increasing fiber density and reducing pore/bubble size while thickening fibers, with only weak influence on segment length. At the network scale, the fitted exponents further imply an emergent packing rule close to pore/bubble size $\propto$ fiber density$^{-1/2}$, providing a simple geometric bridge between connectivity and transport-relevant void structure.

Finally, plasma and purified systems exhibited broadly similar sensitivities (exponents), suggesting a shared underlying assembly mechanism, while the dominant system difference appeared as a shift in the prefactor k, consistent with environment-dependent effective thrombin activity and regulation in plasma. Together, these results provide a predictive scaling atlas and a mechanistically interpretable separation of roles—thrombin setting single-fiber kinetic/length scales and fibrinogen tuning space-filling architecture—useful for theory development and for interpreting how clinically relevant shifts in fibrinogen or thrombin may reshape clot microstructure.

References

1. Weisel, J.W. and R.I. Litvinov, *Mechanisms of fibrin polymerization and clinical implications.* Blood, 2013. **121**(10): p. 1712–1719.
2. Undas, A. and R.A.S. Ariëns, *Fibrin Clot Structure and Function A Role in the Pathophysiology of Arterial and Venous Thromboembolic Diseases.* Arteriosclerosis Thrombosis and Vascular Biology, 2011. **31**(12): p. E88–E99.
3. Danesh, J., et al., *Plasma fibrinogen level and the risk of major cardiovascular diseases and nonvascular mortality - An individual participant meta-analysis.* Jama-Journal of the American Medical Association, 2005. **294**(14): p. 1799–1809.
4. Klovaite, J., et al., *Elevated Fibrinogen Levels Are Associated with Risk of Pulmonary Embolism, but Not with Deep Venous Thrombosis.* American Journal of Respiratory and Critical Care Medicine, 2013. **187**(3): p. 286–293.
5. Charbit, B., et al., *The decrease of fibrinogen is an early predictor of the severity of postpartum hemorrhage.* Journal of Thrombosis and Haemostasis, 2007. **5**(2): p. 266–273.
6. Sidonio, R.J.r., et al., *Thrombin generation and implications for hemophilia therapies: A narrative review.* Research and Practice in Thrombosis and Haemostasis, 2023. **7**(1).
7. Reddel, C.J., C.W. Tan, and V.M. Chen, *Thrombin Generation and Cancer: Contributors and Consequences.* Cancers, 2019. **11**(1).
8. Gehlen, R., et al., *Application of the thrombin generation assay in patients with antiphospholipid syndrome: A systematic review of the literature.* Frontiers in Cardiovascular Medicine, 2023. **10**.
9. Ryan, E.A., et al., *Structural origins of fibrin clot rheology.* Biophysical Journal, 1999. **77**(5): p. 2813–2826.
10. Ferri, F., et al., *Structure of fibrin gels studied by elastic light scattering techniques: Dependence of fractal dimension, gel crossover length, fiber diameter, and fiber density on monomer concentration - art. no. 011913.* Physical Review E, 2002. **66**(1).
11. Belcher, H.A., M. Guthold, and N.E. Hudson, *What is the diameter of a fibrin fiber?* Research and Practice in Thrombosis and Haemostasis, 2023. **7**(5).
12. Risman, R.A., et al., *Comprehensive Analysis of the Role of Fibrinogen and Thrombin in Clot Formation and Structure for Plasma and Purified Fibrinogen.* Biomolecules, 2024. **14**(2).
13. Weisel, J.W., *Structure of fibrin: impact on clot stability.* Journal of Thrombosis and Haemostasis, 2007. **5**: p. 116–124.
14. Pietsch, K., et al., *Correlation between Fibrin Fibrillation Kinetics and the Resulting Fibrin Network Microstructure.* Advanced Healthcare Materials, 2023. **12**(8).
15. Weisel, J.W. and C. Nagaswami, *Computer Modeling of Fibrin Polymerization Kinetics Correlated with Electron-Microscope and Turbidity Observations - Clot Structure and Assembly Are Kinetically Controlled.* Biophysical Journal, 1992. **63**(1): p. 111–128.
16. Kim, O.V., et al., *Structural basis for the nonlinear mechanics of fibrin networks under compression.* Biomaterials, 2014. **35**(25): p. 6739–6749.

17. Cai, C., et al., *Standardization of scanning electron microscopy analysis of fibrin fiber diameter measurement: communication from the ISTH SSC subcommittee on FXIII and fibrinogen.* Journal of Thrombosis and Haemostasis, 2026. **24**(1): p. 318–328.
18. Molteni, M., et al., *Fast Two-Dimensional Bubble Analysis of Biopolymer Filamentous Networks Pore Size from Confocal Microscopy Thin Data Stacks.* Biophysical Journal, 2013. **104**(5): p. 1160–1169.
19. Mickel, W., et al., *Robust Pore Size Analysis of Filamentous Networks from Three-Dimensional Confocal Microscopy.* Biophysical Journal, 2008. **95**(12): p. 6072–6080.
20. Chiu, C.L., et al., *Permeability of Three-Dimensional Fibrin Constructs Corresponds to Fibrinogen and Thrombin Concentrations.* Bioresearch Open Access, 2012. **1**(1): p. 34–40.
21. Kim, O.V., et al., *Fibrin Networks Regulate Protein Transport during Thrombus Development.* Plos Computational Biology, 2013. **9**(6).
22. Muenster, S. and B. Fabry, *A Simplified Implementation of the Bubble Analysis of Biopolymer Network Pores.* Biophysical Journal, 2013. **104**(12): p. 2774–2775.
23. Jesty, J., *The Kinetics of Inhibition of Thrombin by Antithrombin in the Presence of Components of the Hemostatic System.* Blood, 1985. **66**(5): p. 1189–1195.
24. Fogelson, A.L. and J.P. Keener, *Toward an understanding of fibrin branching structure.* Physical Review E, 2010. **81**(5).
25. Li, W., et al., *Nonuniform Internal Structure of Fibrin Fibers: Protein Density and Bond Density Strongly Decrease with Increasing Diameter.* Biomed Research International, 2017. **2017**.